Check for updates

Ni–rGO–zeolite nanocomposite: an efficient heterogeneous catalyst for one-pot synthesis of triazoles in water†

Prasun Choudhury, [ID] [a] Shreyasi Chattopadhyay, [ID] ‡[b] Goutam De [ID] §*[bc] and Basudeb Basu [ID] ¶*[ad]

An important group of pharmaceutical materials, 1,2,3-triazoles, has been synthesised using a Ni-based nanocomposite catalyst (Ni–rGO–zeolite) through azide alkyne cycloaddition (NiAAC). First, a GO–zeolite hybrid was prepared through protonation of a Na–Y–zeolite by H^+ ions originating from the –COOH groups of GO. Subsequently the GO–zeolite was treated with Ni-acetate solvothermally in the presence of $NaBH_4$ (reducing atmosphere). Under the solvothermal conditions a significant part of the incorporated Ni ions in the GO–zeolite were reduced to Ni(0) and simultaneously GO was transformed into rGO. The resulting ternary nanocomposite, Ni–rGO–zeolite, serves as a highly efficient heterogeneous catalyst, and shows excellent regioselectivity forming 1,4-disubstituted-1,2,3-triazoles as the sole product at a low loading of the nickel (∼2.6 mol% with respect to the substrate) with recyclability, and without any significant leaching of the metal. In addition, the Ni–rGO–zeolite exhibits enhanced efficiency under aqueous conditions, proficiency with varying substrates and overcomes some of the shortcomings of the previously reported limited number of Ni-based and other catalysts. The catalytic process is believed to involve the active Ni(0) species, which is stabilized by electron rich rGO that is supported on the microporous high-surface-area zeolite.

1. Introduction

The 1,2,3-triazoles represent an important class of five-membered heterocyclic compounds and they find widespread applications in pharmaceutical, biological chemistry, and drug delivery research.[1–3] The copper(I) catalysed [3+2] cycloaddition (CuAAC) reaction between a terminal alkyne and an alkyl azide, commonly known as the 'click reaction', provides easy access to the regioselective synthesis of 1,4-disubstituted-1,2,3-triazoles.[4] A wide variety of copper catalysts, both homogeneous and heterogeneous forms, have been developed and successfully employed in CuAAC reactions.[5,6] Although copper is cheap and less toxic than many other transition metals, it has some drawbacks in the CuAAC reaction. For example, the intermediate Cu-acetylide tends to polymerize and forms a dinuclear Cu intermediate, eventually affecting the rate of the reaction and the yield of the cycloadduct.[7–10] Moreover, the use of Cu(II) species often requires a reducing agent making the process less atom-economic. Other transition metals like Ru, Rh, Ag, Au, Ir and Zn have also been used as catalysts in AAC,[10–12] though their efficacy is limited in terms of the regioselectivity of the product, general applicability, use of precious metals/ligands and tricky procedure for making the catalytic systems.

The nickel (Ni) catalyzed azide alkyne [3+2] cycloaddition (NiAAC) has rarely been explored and literature reports reveal only a few Ni-based catalysts used in the AAC.[13–16] While the use of Raney® nickel leads to both 1,4- and 1,5-disubstituted cyclo-adducts,[13] the alternative ligand-specific and expensive catalytic system (Cp_2Ni-Xantphos) can be used for both terminal and internal alkynes, preferentially forming 1,5-disubstituted triazoles.[14,15] Moreover, the actual catalyst in this case is Ni (Xantphos)₂, which is generated *in situ* and is not recoverable.[15] Another heterogeneous Ni catalyst is based on the triazole linked organic polymer (Ni-TLOP), which acts as a photocatalyst in AAC

[a] *Department of Chemistry, North Bengal University, Darjeeling 734013, India. E-mail: basu_nbu@hotmail.com*

[b] *CSIR-Central Glass & Ceramic Research Institute, 196, Raja S. C. Mullick Road, Jadavpur, Kolkata 700032, India*

[c] *S. N. Bose National Centre for Basic Sciences, Block – JD, Sector – III, Salt Lake, Kolkata 700106, India. E-mail: g.de@bose.res.in*

[d] *Raiganj University, Raiganj 733134, India*

‡ Present address: School of Chemistry, University of St Andrews, Purdie Building, North Haugh, St. Andrews, Fife KY16 9ST, Scotland, UK.

§ Superannuated from CSIR–Central Glass and Ceramic Research Institute (CSIR–CGCRI), Kolkata.

¶ Present address: Department of Chemistry, Cotton University, Guwahati 781001, India.

under visible light induced conditions.[16] The Ni-TLOP catalyst exhibits a high catalytic performance in AAC, however, preparation of the catalyst requires expensive chemicals, and the catalyst becomes active only under visible light irradiation, as studied in a two-component AAC process. We have previously prepared a Ni catalyst supported on reduced graphene oxide (Ni–rGO) and investigated catalytic performance in C–C and C–S cross coupling reactions.[17,18] Although the rGO surface is rich with a π-electron network for stabilization of the Ni(0) species, we did observe the formation of Ni(II) species being immobilized after the catalytic C–S coupling reaction.[18] Exploring the catalytic performance of Ni–rGO in azide alkyne cycloaddition, however, afforded a poor yield of the cycloadduct (~40%). Microporous zeolites are very attractive for applications as a catalyst,[19] and as support materials for anchoring metal nanoparticles and subsequent catalytic functions.[20] Several unique properties like high surface area, intrinsic nano-sized pore cavities with sub-nano pore openings, easy mass transport properties and also hydrothermal stability make them a versatile host material. We have also prepared Ni–zeolite following the reported procedure,[21] and examined its catalytic performance in three-component AAC. However, the yield of the cycloadduct obtained was only about 52%.

We envisioned that Ni(0) NPs being supported in the high surface area rGO–zeolitic hybrid with a π-electron rich surface could be more useful for the stabilization and subsequent catalytic efficiency of the Ni(0) species. It is known that zeolites consist of a tetrahedral structure with $(AlO_4)^{5-}$ and $(SiO_4)^{4-}$ species, and formal protonation can balance the negative charge resulting hydroxyl bridging (Al–OH–Si), which could serve as the Brønsted acid sites.[19] Again, metal-doped zeolites can have Lewis acidic sites, and tangible synergistic effects of Brønsted–Lewis acidic sites of protonated and metal-doped zeolites could be expected for efficient catalytic applications.[20]

Based on above discussions and considering that graphene oxide (GO) with its peripheral carboxylic acid groups could act as the proton source, we first mixed an aqueous dispersion of GO with NaY zeolite in water to obtain the GO–zeolite hybrid material. Then the hybrid GO–zeolite was treated with nickel(II) salts under reducing conditions to prepare a ternary nanocomposite preferentially with the Ni(0) oxidation state. Characterizations of the material by FT-IR, powder XRD and XPS revealed that the hybrid GO–zeolite is transformed *in situ* to rGO–zeolite anchored with nickel during the impregnation of nickel under reducing conditions to afford the ternary nanocomposite, designated as the Ni–rGO–zeolite. This nanocomposite material, having highly dispersed atomic level active Ni co-hosted by rGO–zeolite is examined as a heterogeneous catalyst in the AAC.

We found that the present heterogeneous catalytic system offers certain advantages, such as easy preparation from cheap and sustainable materials, stability at room temperature, high catalytic efficiency in aqueous medium, regioselective formation of 1,4-disubstituted-1,2,3-triazoles, recovery by simple filtration and recyclability. As compared with previously reported very limited number of homo- and heterogeneous Ni-based catalysts used in the AAC,[13–16] the present catalytic process using Ni–rGO–zeolite follows three-component cycloaddition, which is more advantageous over the two-component cycloaddition process because the former avoids an extra step of making unstable organyl azides (Scheme 1).

2. Results and discussion

2.1. Preparation of Ni–rGO–zeolite nanocomposite

We first prepared a hybrid GO–zeolite from 2D GO and the NaY zeolite (faujasite). The GO–zeolite composite was prepared by adding sodium Y (NaY) zeolite to an aqueous suspension (pH ≈ 11.2) to an aqueous dispersion of GO (pH ≈ 3.4). Addition of the zeolite to the acidic GO solution (where the acid source originates from the carboxylic acid groups associated with GO) increases the pH close to 7 due to protonation. Such protonation balances the negative charges on the zeolite resulting in hydroxyl bridging (Al–OH–Si), which could serve as the Brønsted acid sites. This protonation reaction also helps the formation of a uniform GO–zeolite hybrid. The reaction mixture was then heated at 60 °C for 16 h under gentle magnetic stirring followed by evaporation of water and drying under vacuum to afford the GO–zeolite composite. The GO–zeolite (suspended in ethylene glycol) was subsequently treated with nickel species $(Ni(OAc)_2 \cdot 4H_2O)$ in the presence of $NaBH_4$ under hydrothermal conditions. Under these reaction conditions the *in situ* reduction of GO to rGO and Ni(2+) to Ni(0) occurs, and the ternary nanocomposite material Ni–rGO–zeolite is formed (see Experimental section for details). The ternary
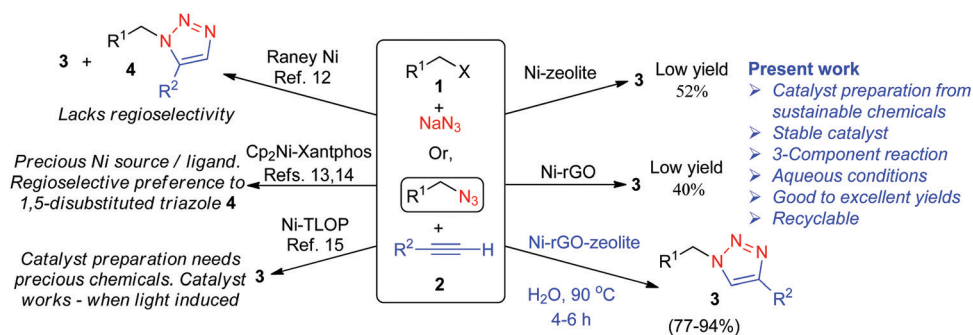
Scheme 1 Comparative scheme for various Ni-catalysed azide alkyne cycloadditions either in two- or three-component processes.

nanocomposite material has been characterized using various spectroscopic and microscopic techniques.

2.2. Characterization of Ni–rGO–zeolite nanocomposite

2.2.1. ICP-AES analysis. The presence of nickel in the ternary nanocomposite was measured by inductively coupled plasma atomic emission spectroscopy (ICP-AES). For this purpose, the nanocomposite catalyst (5 mg) was digested with aqua regia (6 mL) and the nickel content was estimated to be 0.887 mmol g^{-1} of the Ni–rGO–zeolite nanocomposite.

2.2.2. FT-IR spectral analysis. The FT-IR spectra of the Ni–rGO–zeolite, GO–zeolite, NaY zeolite and only GO were recorded and are presented in Fig. 1. In the case of GO, the peaks at 1729 and 1627 cm^{-1} were due to the stretching vibrations of C=O and C=C bonds respectively.[22] The broad peak at around 3432 cm^{-1} was related to the stretching vibration of the hydroxyl groups present in GO.[22] In the case of the GO–zeolite and the Ni–rGO–zeolite, the peaks at 1022, 578 and 454 cm^{-1} were due to the internal vibrations of the TO$_4$ (T = Si, Al) tetrahedral moiety of the NaY zeolite.[23] Moreover, the disappearance of the typical carbonyl band at 1729 cm^{-1} indicates that the carbonyl groups might have been converted to Al/Si–O–C bonds resulting in the formation of the nanocomposite.[24]

2.2.3. Raman spectral analysis. It is noteworthy to mention that the transformation of GO to rGO is expected during the hydrothermal treatment of the GO–NaY hybrid during incorporation with nickel. Therefore, a Raman spectral analysis was performed and analysed (Fig. 2). The presence of D and G bands along with the 2D related bands in the Raman spectrum of the nanocomposite (Fig. 2) conform to the transformation of GO to rGO. The Raman spectrum of the GO–NaY composite shows a sharp 2D peak with the obvious presence of the D and G bands. As expected, the higher intensity of the G band (I_G) over that of the D band (I_D) was observed. Whereas, after the hydrothermal treatment the intensity of the D band was not
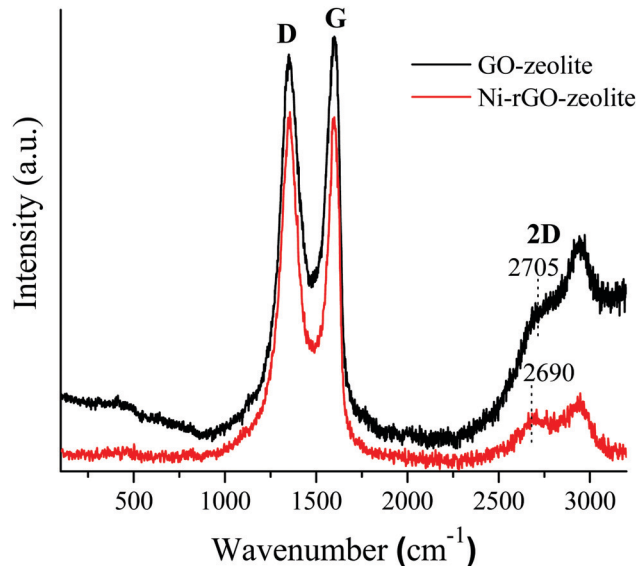

Fig. 2 Raman spectra of the Ni–rGO–zeolite catalyst and GO–zeolite (as control).

only increased ($I_D/I_G > 1$) but also the 2D band (which appeared at 2705 cm^{-1} in the case of GO–NaY) was shifted slightly towards a lower wavenumber at 2690 cm^{-1} (Fig. 2). Such observations corroborate the transformation of GO to rGO *via* reformation of graphitic regions in the sheet.[25]

2.2.4. Powder XRD analysis. The XRD peaks of the Ni–rGO–zeolite nanocomposite (Fig. 3) can be assigned to the reflection of the NaY zeolite crystal planes, and thus confirm the existence of the zeolite phase.[26] The XRD pattern of the nanocomposite catalyst has been compared with that of GO–zeolite as the control sample, where similar patterns reveal the retention of the NaY crystal structure after incorporation of Ni in the composite system. A similar trend of the I_{220} and I_{311} peaks (inset of Fig. 3) in both the cases also indicated that there was probably no encapsulation of Ni in the NaY zeolite cage.[27] However, chemical characteristics of Ni component could not

Fig. 1 FT-IR spectra of GO, NaY zeolite, GO–zeolite and Ni–rGO–zeolite.

Fig. 3 XRD patterns of GO–zeolite and Ni–rGO–zeolite composites.

be detected, presumably due to the strong presence of NaY zeolite reflection peaks in the pattern.

2.2.5. XPS analysis. The X-ray photoelectron spectroscopy (XPS) survey scan of the catalyst (Ni–rGO–zeolite) shows binding energy peaks of Al2p, Si2p, and Na1s corresponding to the zeolite, C1s from rGO, and Ni2p from the Ni NPs (Fig. 4a). For detailed analysis, deconvolution of the high resolution C1s and Ni2p spectra was undertaken to check the interaction between rGO and Ni. The deconvoluted C1s spectrum (Fig. 4b) showed binding energy peaks corresponding to C=C (284.42 eV) and C–C (285.08 eV) arising from rGO. In addition, peaks at 285.90, 287, 287.75 and 289 eV indicated the presence of C–OH, C–O–C, C=O and O=C–O functional groups on rGO, respectively.[28] Moreover, the peak appearing at 286.50 eV can be attributed to the Ni–C bonding. The Ni2p high resolution spectrum shows the $Ni2p_{1/2}$ and $Ni2p_{3/2}$ core-level signals (Fig. 4c). In this spectrum, the existence of the $Ni2p_{3/2}$ and $Ni2p_{1/2}$ core-level peaks at 853.17 and 870.54 eV, respectively, corresponds to the free metallic Ni(0).[29,30] The pair of binding energy peaks at 856.95 ($Ni2p_{3/2}$) and 874.46 ($Ni2p_{1/2}$), and 862.68 eV ($Ni2p_{3/2}$) and 880.80 eV ($Ni2p_{1/2}$) can be assigned to Ni–O–C and Ni–C bonds, respectively.[29,30] Therefore, the XPS results confirmed the existence of the intrinsic interaction between the rGO and Ni moieties.

2.2.6. SEM and TEM analysis. The morphology and microstructure of the as-prepared Ni–rGO–zeolite was analyzed using scanning electron microscopy (SEM). Comparison of the SEM images for GO–zeolite and Ni–rGO–zeolite revealed the existence of crystal aggregates of the zeolites along with GO/rGO (Fig. 5a and b). The basic agglomerated structure of both materials looks similar. In the Ni–rGO–zeolite nanocomposite, the Ni species should be uniformly dispersed on the rGO/zeolite surface through chemical interaction between the functional groups of rGO and zeolite crystals. Clearly the agglomerated structure composed of plate-like crystals interconnected with the rGO (see the magnified view shown in the inset of Fig. 5b) is seen. Energy dispersive X-ray scattering analysis (SEM-EDS) of the Ni–rGO–zeolite confirmed the presence of Ni along with other elements C, O, Si, Na and Al (originating from rGO and the zeolite) in the nanocomposite (Fig. 5c). The transmission electron microscopy (TEM) image of the Ni–rGO–zeolite nanocomposite (Fig. 6) shows good distribution of the quasi hexagonal plate-like nanostructures of the zeolites with rGO sheets (see the magnified view for better understanding).[31] The XPS analysis has confirmed that a significant amount of the nickel is bonded with the functional groups (ionic state/Ni^{2+}), as well as the existence of metallic nickel (Ni^0). Although the visibility of metallic nickel in the TEM image is not clear, the SEM-EDS analysis confirmed the existence of Ni (1.29 wt%) in the nanocomposite.

3. Catalytic activity of Ni–rGO–zeolite nanocomposite

3.1. Catalytic activity

In order to evaluate the catalytic activity of this newly developed ternary nanocomposite (Ni–rGO–zeolite) in a three-component
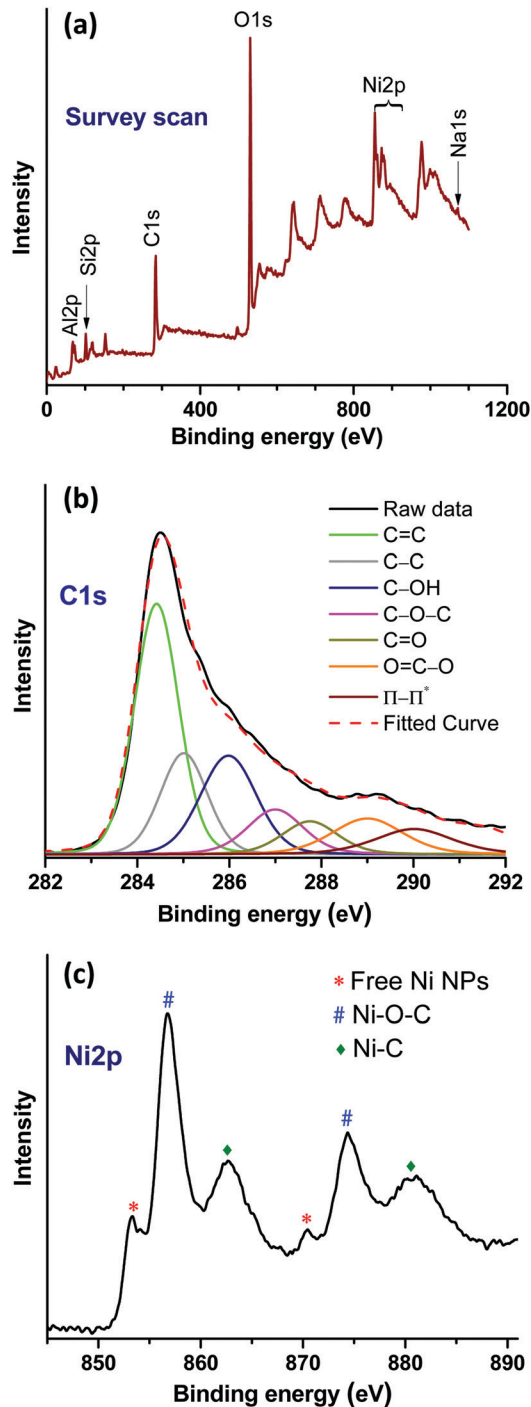

Fig. 4 XPS studies of freshly prepared Ni–rGO–zeolite catalyst. (a) Survey scan, (b) high resolution C1s, and (c) high resolution Ni2p spectra.

azide–alkyne 'click' reaction for the synthesis of triazole moieties, we examined the combination of benzyl bromide (**1a**), phenylacetylene (**2a**) and sodium azide as the model reactants, and the results are presented in Table 1. As described above, we carried out the reaction using the heterogeneous catalytic systems Ni–rGO and Ni–zeolite in aqueous medium at 90 °C (entries 1 and 2), which gave the desired cycloadduct in 40% and 52% yields, respectively. The use of our newly
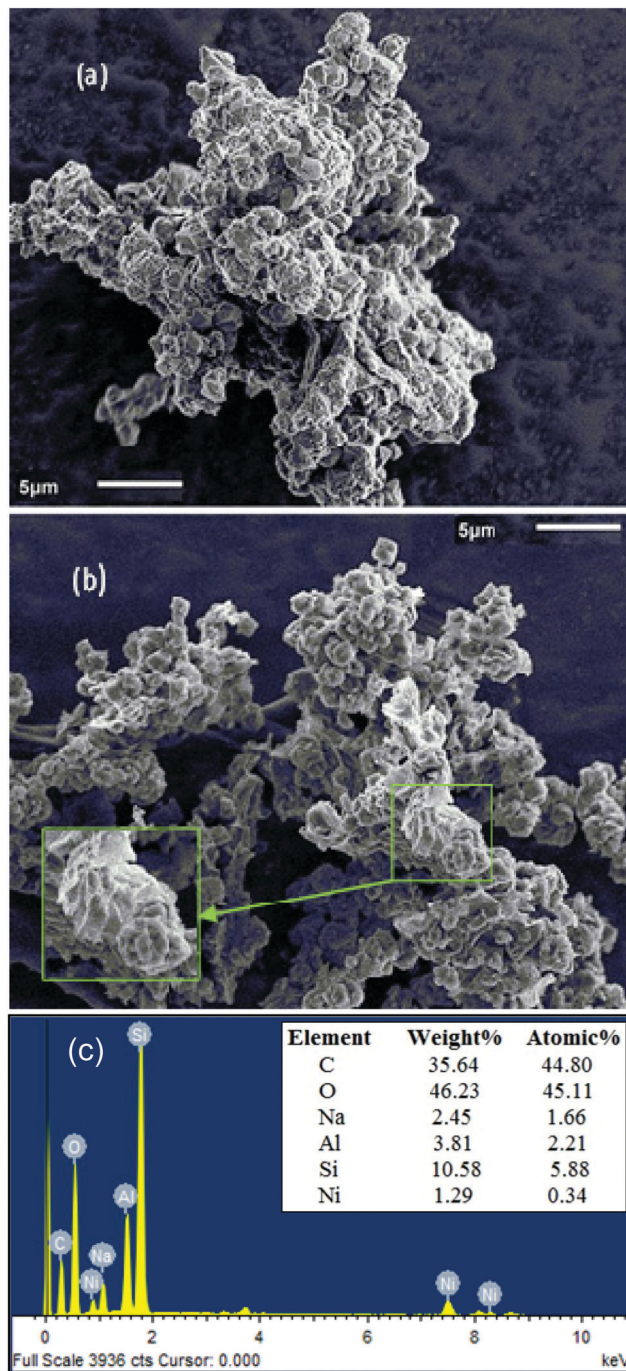
Fig. 6 TEM image of Ni–rGO–zeolite. A magnified view of a selected area in the yellow square is also shown.

performed the reaction in the presence of an additive, tetra-butylammonium bromide (TBAB, 10 mol%), but observed a fairly similar result (95%; entry 7). We also checked the viability of the catalytic reaction in organic solvent (CH_3CN) or in a mixture of $CH_3CN:H_2O$ (1:1 v/v) at 80 °C, which gave the desired product **3a**, respectively, in 67% and 81% yield (entries 8 and 9). We also screened the reaction in organic solvents like methanol (MeOH) and dimethylformamide (DMF), both protic and aprotic polar solvents. While the reaction in MeOH at 90 °C afforded the desired product **3a**, in 83% yield (entry 10), the same reaction in DMF at 110 °C for 4 h and 10 h gave **3a** in 88% and 90% yield, respectively (entries 11 and 12). The use of the polar aprotic solvent (DMF) gave slightly better conversions

Fig. 5 SEM images of (a) GO–zeolite, (b) Ni–rGO–zeolite, and (c) representative EDS spectrum of Ni–rGO–zeolite, elemental composition is shown in the inset (average values of 3 sets of EDS data).

developed catalyst (Ni–rGO–zeolite; 30 mg mmol^{-1} of benzyl bromide) afforded the product (1-benzyl-4-phenyl-1H-1,2,3-triazole; **3a**) in 94% yield under similar conditions (entry 3). Reducing the amount of catalyst to 15 mg however lowered the yield of the product (82%; entry 4). Again, lowering the temperature also gave **3a** in 69% yield only (entry 5). When a neat mixture of the reactants and catalyst was used for the reaction, we isolated the product in 77% yield (entry 6). We also
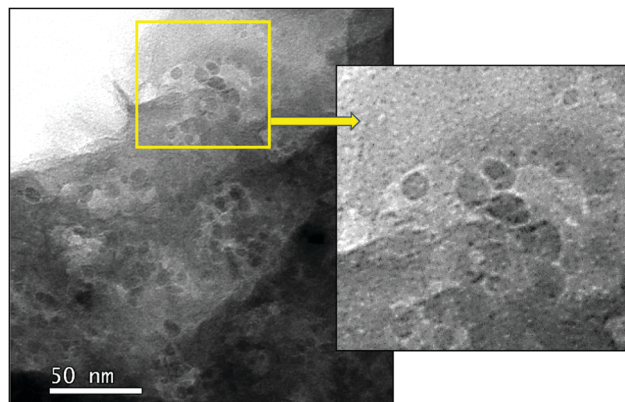
Table 1 Optimization of the reaction conditions[a]

Entry	Catalyst (mg)	Solvent	Temp (°C)/time (h)	Yield[b] (%)
1	30	H_2O	90/4	40[c]
2	30	H_2O	90/4	52[d]
3	**30**	**H_2O**	**90/4**	**94[e]**
4	15	H_2O	90/4	82
5	30	H_2O	60/4	69
6	30	—	90/4	77
7	30	H_2O	90/4	95[f]
8	30	CH_3CN	80/4	67
9	30	$CH_3CN:H_2O$ (1:1)	80/4	81
10	30	MeOH	90/4	83
11	30	DMF	110/4	88
12	30	DMF	110/10	90
13	$Ni(OAc)_2\cdot4H_2O$	H_2O	90/4	53[g]
14	—	H_2O	80/24	16
15	100	H_2O	90/4	89

[a] Reaction conditions: **1a** (1 mmol), **2a** (1 mmol), NaN$_3$ (1.5 mmol) and solvent (2 mL). [b] Isolated yield. [c] Reaction carried out using the Ni–rGO catalytic system (the FT-IR spectrum of Ni–rGO is given in the ESI, Section SI-2.1 and Fig. S1). [d] Reaction carried out using the Ni–zeolite catalytic system (the FT-IR spectrum of Ni–zeolite is given in the ESI, Section SI-2.2 and Fig. S2). [e] Reaction carried using Ni–rGO–zeolite. [f] TBAB (10 mol%) was used. [g] $Ni(OAc)_2\cdot4H_2O$ (15 mol%) was used.

over protic MeOH as the solvent, though the prolonged reaction time (10 h) in DMF did not show any significant improvement in terms of yield of the desired product **3a**. Further studies with Ni(OAc)$_2$·4H$_2$O as the catalyst (15 mol%) could produce the cycloadduct in 53% yield under similar reaction conditions (entry 13), whereas the reaction conducted in the absence of any catalyst resulted in a meagre conversion (16%; entry 14). This finding suggested the significant role of the Ni catalyst in the three-component [3+2] AAC. Studies under various conditions suggested the optimal conditions were as in entry 3. Finally, we scaled up the reaction under the optimized conditions with a partially lowered loading of the catalyst and that also resulted in a good conversion (entry 15, 89%).

The general applicability of the catalyst was examined with various alkyl halides and terminal alkynes using the optimized conditions (Table 2). Initially, we varied alkyl halides for the reaction, keeping the alkyne fixed. Subsequently, we tested the effect of the substituent on the alkyne partner for the reaction. Both benzyl bromide and benzyl chloride gave the triazole **3a** in 94% and 90% isolated yield respectively. Benzyl bromide bearing an isopropyl, bromo or iodo group in the ring reacted efficiently with phenylacetylene affording the desired products (**3b–3d**) in 88–91% yield. In case of cinnamyl bromide, although the reaction took place affording the triazole **3e**, the yield of the

product was comparatively low. The lower yield might be due to the tendency of cinnamyl azide to undergo an intramolecular rearrangement.[32] Alkyl halide containing the naphthyl group, for example, 1-chloromethyl naphthalene, also reacted under the conditions giving product **3f** in 85% yield. A further attempt with allyl bromide also worked smoothly and the desired product **3g** was obtained in 83% isolated yield. The reaction involving activated functionalized organic halides, such as 4-chlorophenacyl bromide, was also accomplished. Terminal alkynes other than phenylacetylene, such as 4-ethynyltoluene, 1-bromo-4-ethynylbenzene and 1-ethynyl-4-nitrobenzene, also reacted efficiently. In the reaction between 4-ethynyltoluene and different alkyl halides, under the standard reaction conditions, the corresponding triazoles (**3i–3m**) were obtained in 78–94% yield. 1-Bromo-4-ethynylbenzene and 1-ethynyl-4-nitrobenzene were also transformed into the corresponding triazoles (**3n** and **3o**) in 87% and 80% yield respectively. We further extended the product library of triazoles bearing strong electron donating (on the alkynyl part) and strong electron withdrawing groups (on the alkyl halide part) and the corresponding triazole products (**3p** and **3q**) were obtained in 91% and 87% isolated yields respectively. Thus the reaction conditions are robust, regioselective and green regardless of the electronic nature and substitution pattern on the alkyl as well as the alkyne moiety. We present a comparative table (Table S1, ESI†) which consists of the catalytic performances (such as loading, general applicability and other aspects) of the present catalytic system, Ni–rGO–zeolite nanocomposite, with reported Ni–, Cu– and other transition metal-based catalysts in the AAC reaction. The comparative table shows the advantages of our catalyst, Ni–rGO–zeolite, as compared with the state-of-the-art reports.

We have reported the preparation of a heterogeneous copper catalyst (Cu$_2$O@ARF) and its application in a three-component azide alkyne cycloaddition reaction.[6] We considered that it is worth comparing the relative catalytic performance between the copper catalyst (Cu$_2$O@ARF) and the present catalytic system

Table 2 Ni–rGO–zeolite catalysed three-component click reaction in water^a
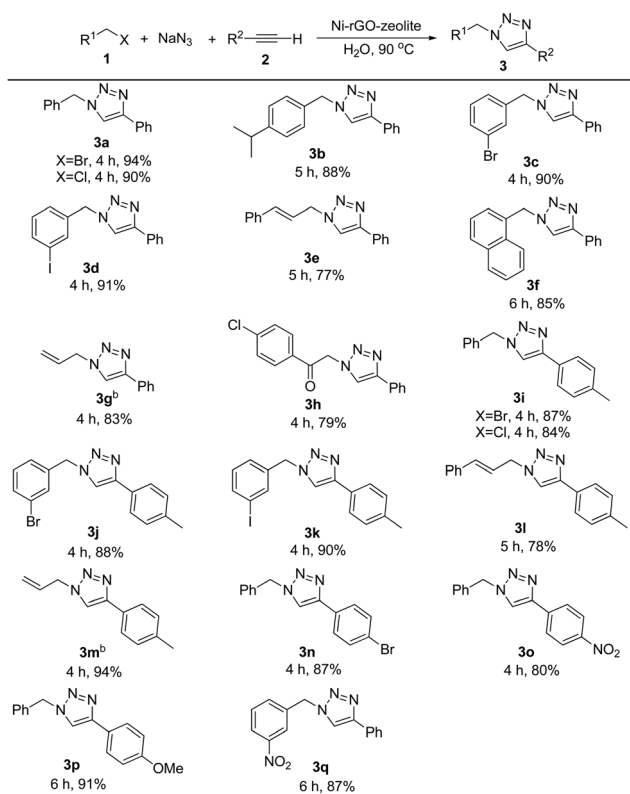
^{a} Reaction conditions: **1** (1 mmol), **2** (1 mmol), NaN$_3$ (1.5 mmol), Ni–rGO–zeolite (30 mg) and H$_2$O (2 mL) were stirred at 90 °C. ^{b} Reaction was carried out at 70 °C.
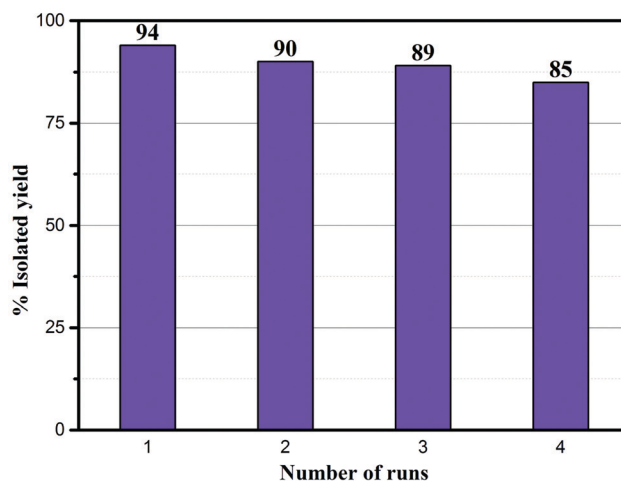

Fig. 7 Recycling experiments using the Ni–rGO–zeolite in the click reaction between benzyl bromide, NaN$_3$ and phenylacetylene.
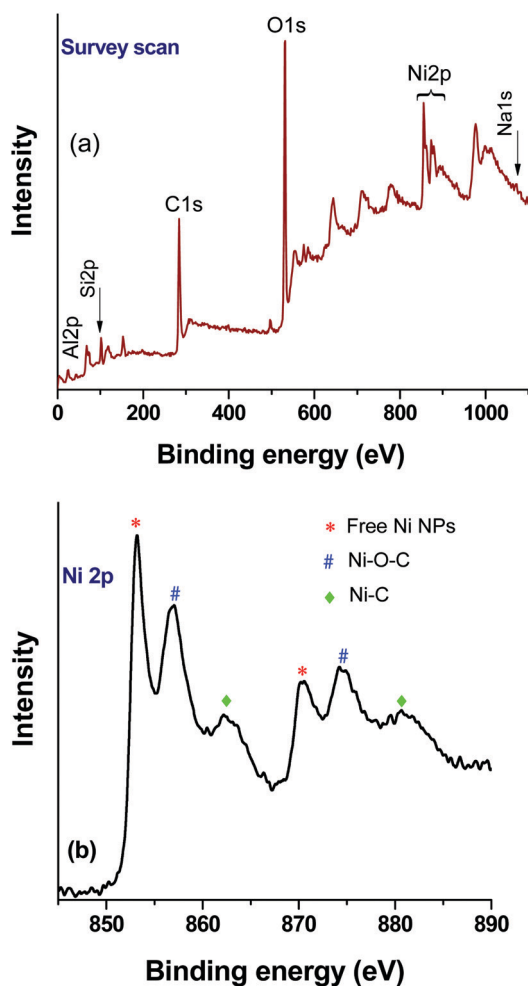
Fig. 8 XPS analysis of the Ni–rGO–zeolite composite catalyst after the first run: (a) survey scan and (b) high resolution Ni2p spectrum.

(Ni–rGO–zeolite). The results show relatively better yields in most of the representative examples in the NiAAC, indicating that suitably designed and stabilized Ni(0) catalysts are quite efficient in three-component azide alkyne cycloaddition giving rise to the regioselective formation of 1,4-disubstituted triazoles (Table S2, ESI†).

3.2. Recyclability of Ni–rGO–zeolite nanocomposite

The recyclability of the Ni–rGO–zeolite catalyst was evaluated in the three-component reaction of **1a**, **2a** and NaN_3 in water under the optimized conditions (Table 1, entry 3). After the first run the catalyst was separated by simple filtration, washed with ethyl acetate (5 × 5 mL) and dried under vacuum for 24 h and was re-used for the second run. In the same process, the catalyst was re-used for four consecutive runs without any significant drop in the yield of the product (Fig. 7). A small drop in yield is due to loss of the catalyst during its isolation after each cycle of reaction. We measured the nickel content in the Ni–rGO–zeolite before and after the recycling runs. As seen from ICP-AES measurements, before the reaction the nickel content in the Ni–rGO–zeolite was 0.887 mmol g^{-1}, whereas after the first and third runs the nickel content was 0.887 mmol g^{-1}, and 0.733 mmol g^{-1}, respectively. This indicates that no significant leaching of nickel occurred from the nanocomposite during the reaction. Detailed characterizations (FT-IR, XRD and Raman) of the Ni–rGO–zeolite catalysts after recycling experiments are given in the ESI† (Section SI-3 and Fig. S3–S5). All these characterizations confirm that the developed nanocomposite catalyst (Ni–rGO–zeolite) is stable after reaction.

3.3. XPS analysis of the catalyst after the reaction

XPS analysis of the catalyst after the first cycle was carried out to understand any changes in the chemical state of the elements (nickel) (Fig. 8). The survey scan (Fig. 8a) shows that binding energy peaks originating from the rGO, zeolite and Ni were observed. However, in the Ni2p high resolution spectrum, an increase of metallic Ni NPs related peaks was observed (Fig. 8b). As a result, the relative peak intensities of Ni–O–C and Ni–C were decreased. It is noteworthy that, under the reaction conditions, NaN_3 has the ability to modify the oxygen containing functional groups of rGO,[33] and as such the formation of a greater number of free nickel NPs in the composite after the first cycle of the reaction could be expected. However, the ICP-AES analysis confirmed the retention of the total nickel content in the composite catalyst, and thus no significant loss during catalysis was observed in the subsequent reactions.
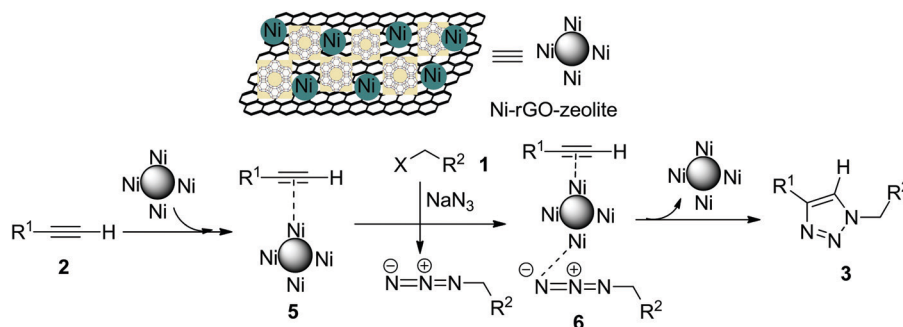
Scheme 2 Plausible mechanism for the Ni–rGO–zeolite catalysed click reaction (NiAAC).

3.4. Plausible mechanism for the reaction

The Cu-catalysed cycloaddition (CuAAC) is believed to involve copper acetylide as one of the key intermediates, which then undergoes cycloaddition with the azide moiety leading to the formation of the triazole (the Sharpless–Meldal version of the CuAAC reaction).[7–9] However, Sommer et al. observed that a similar reaction on the Cu[I]–zeolite surface does not involve the Cu–acetylide intermediate and proceeds through the formation of a π-complex between alkyne and the metal ion anchored with the zeolite followed by reaction with the azide and subsequent formation of the triazole.[34] When Raney® nickel is used as the catalyst, the AAC reaction (NiAAC) is also believed to occur through π-complexation between the alkyne and nickel followed by cycloaddition with the azide. The author studied the reaction with a terminal deuterated alkyne and obtained the triazole with complete retention of deuterium.[13] Based on these observations, we consider that the free nickel NPs, being confined in the zeolitic pores and supported by rGO, could be the active catalyst for the cycloaddition reaction. The first step of the reaction presumably involves a Ni(0) coordinated alkyne species (**5**), which then coordinates with the in situ generated alkyl azide to form (**6**) (Scheme 2). The stabilized Ni(0) NPs supported with the rGO–zeolite help to bring the reacting partners closer for undergoing regioselective cycloaddition that leads to the formation of the triazole (**3**).

4. Conclusion

In conclusion, we have developed a new Ni-based ternary nanocomposite material that exhibits excellent catalytic activity in the three-component azide alkyne cycloaddition (NiAAC) in water, leading to the regioselective formation of 1,4-disubstituted 1,2,3-trizole. The heterogeneous catalyst (Ni–rGO–zeolite) is easy to prepare, robust, and recyclable without any significant drop in its performance. The partly enhanced catalytic performance of this heterogeneous Ni catalyst in AAC presumably originates from the concurrent support and stabilization of the active Ni(0) species by a unique combination of microporous zeolitic pores being supported with the π-electron-rich rGO surface. Among the very few Ni catalysts studied in the [3+2] AAC, the present catalytic system not only eliminates some of the shortcomings but will certainly pave the way for further application of Ni-catalysed 'click' reactions.

5. Experimental section

(see also ESI;† SI-1).

5.1. Preparation of graphene oxide (GO)

Graphene oxide was prepared by following Tour's method.[22] In this method a 9:1 (v/v) mixture of H_2SO_4/H_3PO_4 (180:20 mL) was added to a mixture of graphite powder (1.5 g) and $KMnO_4$ (9.0 g). The mixture was then stirred at 50 °C for 12 h. After cooling the mixture to room temperature, it was gradually poured into crushed ice (200 g), which was followed by the slow addition of H_2O_2 (30%, 3 mL). The solution was then centrifuged (5000 rpm) and the supernatant was discarded. The residual solid material was successively washed with deionised water (100 mL) and then with 30% HCl (100 mL). The solid material was then repeatedly washed with water and centrifuged. Finally, the solid brown material was collected and dried at 60 °C under vacuum to obtain solid graphene oxide.

5.2. Preparation of GO–zeolite nanocomposite

Graphene oxide (275 mg) was dispersed in distilled water (100 mL) and ultrasonically treated for 1 h. Subsequently, sodium Y zeolite (400 mg) was steadily added to the GO dispersion to ensure the neutral pH of the overall dispersion. The dispersion was then heated using an oil bath at 60 °C with stirring for 16 h. The solvent was then removed under reduced pressure and the solid mass was dried under vacuum for 24 h.

5.3. Preparation of Ni–rGO–zeolite nanocomposite

A Teflon capped sealed tube containing the GO–zeolite (500 mg) dispersion in ethylene glycol (10 mL) was charged with $Ni(OAc)_2\cdot 4H_2O$ (124 mg, 0.5 mmol). The contents were then gently stirred at 60 °C for 30 minutes. After that, $NaBH_4$ (37 mg, 1 mmol) was added to the mixture portion wise. The sealed tube was again Teflon capped and placed in a preheated oil bath at 180 °C. After stirring for 3 h, the mixture was cooled to room temperature, diluted with water and centrifuged at 5000 rpm. The supernatant was discarded and the solid composite material was washed alternatively with water and ethanol (3 times each). The solid composite material was then dried under vacuum for 48 h.

5.4. Preparation of Ni–zeolite and Ni–rGO catalysts (control samples)

The Ni–zeolite composite catalyst was prepared using a reported literature method with minor modifications.[21] Briefly, a 250 mL RB flask was charged with ethylene glycol (50 mL) and $NiNO_3\cdot 6H_2O$ (290 mg). The mixture was ultrasonicated for 30 min, sealed, purged with nitrogen and placed in an oil bath at 200 °C. This was followed by the rapid addition of $NaBH_4$ (200 mg) into the flask. The mixture was then stirred at this temperature for 2 h before being cooled to room temperature. The solid was separated by centrifugation, washed with ethanol and distilled water (3 times each) and dried under vacuum for 24 h. The other control sample, the Ni–rGO catalyst, was prepared following our previously reported method.[18] These catalysts were verified by FT-IR analysis (ESI,† Section SI-2).

5.5. General procedure for the synthesis of 1,4-disubstituted-1,2,3-triazole derivatives using Ni–rGO–zeolite catalyst

A round bottomed flask (25 mL) equipped with a magnetic stir bar was charged with alkyl halide (1 mmol), terminal alkyne (1 mmol), NaN_3 (1.5 mmol) and the Ni–rGO–zeolite (30 mg). Freshly distilled water (2 mL) was added to it and the reaction mixture was gently stirred at 90 °C for 4–6 h. After completion of the reaction (monitored by TLC), the reaction mixture was cooled to room temperature. The catalyst was recovered through simple filtration and the reaction mixture was

extracted using ethyl acetate (3 × 5 mL). The combined organic layer was dried over anhydrous Na_2SO_4 and concentrated under vacuum. The residue obtained was purified by column chromatography using light petroleum ether/ethyl acetate as the eluent to afford the desired product. All products were characterized by ^1H, and ^{13}C-NMR data and were also compared with reported melting points for solid compounds (ESI;† Sections SI-4 and SI-5).

Conflicts of interest

There are no conflicts to declare.

Acknowledgements

Notes and references

1 K. Bozorov, J. Zhao and H. A. Aisa, *Bioorg. Med. Chem.*, 2019, **27**, 3511–3531.
2 S. Guernelli, A. Cariola, A. Baschieri, R. Amorati and P. L. Meo, *Mater. Adv.*, 2020, **1**, 2501–2508.
3 D. Dheer, V. Singh and R. Shankar, *Bioorg. Chem.*, 2017, **71**, 30–54.
4 N. Nebra and J. Garcia-Alvarez, *Molecules*, 2020, **25**, 2015–2033.
5 S. Neumann, M. Biewend, S. Rana and W. H. Binder, *Macromol. Rapid Commun.*, 2020, **41**, 1900359.
6 S. Ghosh, S. Saha, D. Sengupta, S. Chattopadhyay, G. De and B. Basu, *Ind. Eng. Chem. Res.*, 2017, **56**, 11726–11733.
7 R. Chung, A. Vo, V. V. Fokin and J. Hein, *ACS Catal.*, 2018, **8**, 7889–7897.
8 L. Zhu, C. J. Brassard, X. Zhang, P. M. Guha and R. J. Clark, *Chem. Rec.*, 2016, **16**, 1501–1517.
9 B. T. Worell, J. A. Malik and V. V. Fokin, *Science*, 2013, **340**, 457–460.
10 C. Wang, D. Ikhlef, S. Kahlal, J.-Y. Saillard and D. Astruc, *Coord. Chem. Rev.*, 2016, **316**, 1–20.
11 M. A. Morozova, M. S. Yusubov, B. Kratochvil, V. Eigner, A. A. Bondarev, A. Yoshimura, A. Saito, V. V. Zhdankin, M. E. Trusova and P. S. Postnikov, *Org. Chem. Front.*, 2017, **4**, 978–985.
12 J. R. Johansson, T. Beke-Somfai, A. Said Stålsmeden and N. Kann, *Chem. Rev.*, 2016, **116**, 14726–14768.
13 H. S. P. Rao and G. Chakibanda, *RSC Adv.*, 2014, **4**, 46040–46048.
14 W. G. Kim, M. E. Kang, J. B. Lee, M. H. Jeon, S. Lee, J. Lee, B. Choi, P. M. Cal, S. Kang and J.-M. Kee, *J. Am. Chem. Soc.*, 2017, **139**, 12121–12124.
15 W. G. Kim, S.-y. Baek, S. Y. Jeong, D. Nam, J. H. Jeon, W. Choe, M.-H. Baik and S. Y. Hong, *Org. Biomol. Chem.*, 2020, **18**, 3374–3381.
16 D. Yadav, N. Singh, T. W. Kim, J. Y. Kim, N.-J. Park and J.-O. Baeg, *Green Chem.*, 2019, **21**, 2677–2685.
17 K. Bhowmik, D. Sengupta, B. Basu and G. De, *RSC Adv.*, 2014, **4**, 35442–35448.
18 D. Sengupta, K. Bhowmik, G. De and B. Basu, *Beilstein J. Org. Chem.*, 2017, **13**, 1796–1806.
19 M. Ravi, V. L. Sushkevich and J. A. van Bokhoven, *Nat. Mater.*, 2020, **19**, 1047–1056.
20 W. Luo, W. Cao, P. C. A. Bruijnincx, L. Lin, A. Wang and T. Zhang, *Green Chem.*, 2019, **21**, 3744–3768.
21 K. Guo, Y. Zhang, Q. Shi and Z. Yu, *Energy Fuels*, 2017, **31**, 6045–6055.
22 D. C. Marcano, D. V. Kosynkin, J. M. Berlin, A. Sinitskii, Z. Sun, A. Slesarev, L. B. Alemany, W. Lu and J. M. Tour, *ACS Nano*, 2010, **4**, 4806–4814.
23 M. Khatamian, B. Divband and F. Farahmand-Zahed, *Mater. Sci. Eng., C*, 2016, **66**, 251–258.
24 W. L. Zhang and H. J. Choi, *Langmuir*, 2012, **28**, 7055–7062.
25 W. Ruan, J. Hu, J. Qi, Y. Hou, R. Cao and X. Wei, *Materials*, 2018, **11**, 865.
26 S. L. Hailu, B. U. Nair, M. Redi-Abshiro, R. Aravindhan, I. Diaz and M. Tessema, *RSC Adv.*, 2015, **5**, 88636–88645.
27 S. C. Mohan, R. V. Solomon, P. Venuvanalingam and K. Jothivenkatachalam, *New J. Chem.*, 2017, **41**, 9505–9512.
28 S. Chattopadhyay, S. Maiti, I. Das, S. Mahanty and G. De, *Adv. Mater. Interfaces*, 2016, **3**, 1600761.
29 C. Zhou, J. A. Szpunar and X. Cui, *ACS Appl. Mater. Interfaces*, 2016, **8**, 15232–15241.
30 F. Yang, M. Wang, W. Liu, B. Yang, Y. Wang, J. Luo, Y. Tang, L. Hou, Y. Li, Z. Li, B. Zhang, W. Yang and Y. Li, *Green Chem.*, 2019, **21**, 704–711.
31 P. Gebhardt, S. W. Pattinson, Z. Ren, D. J. Cooke, J. A. Elliott and D. Eder, *Nanoscale*, 2014, **6**, 7319–7324.
32 A. K. Feldman, B. Colasson, K. B. Sharpless and V. V. Fokin, *J. Am. Chem. Soc.*, 2005, **127**, 13444–13445.
33 R. Salvio, S. Krabbenborg, W. J. Naber, A. H. Velders, D. N. Reinhoudt and W. G. van der Wiel, *Chem. – Eur. J.*, 2009, **15**, 8235–8240.
34 S. Chassaing, A. Sani Souna Sido, A. Alix, M. Kumarraja, P. Pale and J. Sommer, *Chem. – Eur. J.*, 2008, **14**, 6713–6721.